

HIGH-VELOCITY TYPE IA SUPERNOVA HAS A UNIQUE HOST ENVIRONMENT

YEN-CHEN PAN^{1,2}*Draft version February 2, 2022*

ABSTRACT

Ejecta velocity of type Ia supernovae (SNe Ia) is one powerful tool to differentiate between progenitor scenarios and explosion mechanisms. Here we revisit the relation between photospheric Si II $\lambda 6355$ velocities ($v_{\text{Si II}}$) and host-galaxy properties with ~ 280 SNe Ia. A more stringent criterion on the phase of SN spectra is adopted to classify SNe Ia in terms of their photospheric velocities. We find significant trend that SNe Ia with faster Si II $\lambda 6355$ (high- $v_{\text{Si II}}$ SNe Ia) tend to explode in massive environments, whereas their slower counterparts can be found in both lower-mass and massive environments. This trend is further supported by the direct measurements on host gas-phase metallicities. We suggest this relation is likely caused by at least two populations of SNe Ia. Since stars of higher metallicity (at a given mass) generally form less massive white dwarfs (WDs), our results support some theoretical models that high- $v_{\text{Si II}}$ SNe Ia may originate from sub-Chandrasekhar class of explosions. Previous observations also showed some evidence that high- $v_{\text{Si II}}$ SNe Ia could be related to the single degenerate systems. However, we find high- $v_{\text{Si II}}$ SNe Ia do not come from particularly young populations. We conclude metallicity is likely the dominant factor in forming high- $v_{\text{Si II}}$ SNe Ia. This also implies their potential evolution with redshift and impact on the precision of SN Ia cosmology.

1. INTRODUCTION

Type Ia supernovae (SNe Ia) are believed to be the result of the thermonuclear explosion of an accreting carbon-oxygen white dwarf (WD) star in a close binary system (Nugent et al. 2011; Bloom et al. 2012). However, the nature of the companion star that donates material is not yet clear. The various possibilities include the single degenerate (Whelan & Iben 1973) and double degenerate (Iben & Tutukov 1984; Webbink 1984) scenarios, as well as more variations on these themes (for recent reviews, see Hillebrandt & Niemeyer 2000; Hillebrandt et al. 2013; Maoz et al. 2014).

The host galaxies of SNe Ia has long been a profitable route to probe the SN Ia population, with the observed properties of SNe Ia known to correlate with the physical parameters of their host galaxies. Previous studies have found significant correlations between SN Ia light curve parameters and luminosities, and the properties of their host galaxies (e.g., Kelly et al. 2010; Lampeitl et al. 2010; Sullivan et al. 2010; D’Andrea et al. 2011; Johansson et al. 2013; Childress et al. 2013; Pan et al. 2014). SNe Ia with faster light curves are preferentially resided in massive and metal-rich galaxies than those in lower-mass and metal-poor systems. Galaxies with stronger star-formation and younger populations tend to host slower and brighter SNe Ia than passive and older galaxies.

Previous studies also showed some evidence that the SN Ia spectral features correlate with the host properties. By dividing SNe Ia into two sub-groups according to their photospheric velocities, Wang et al. (2013) found SNe Ia with high Si II $\lambda 6355$ velocities (high- $v_{\text{Si II}}$ SNe Ia, defined as $v_{\text{Si II}} \gtrsim 12,000 \text{ km s}^{-1}$; Wang et al. 2009) tend to be more concentrated in the inner regions of their host galaxies, whereas the normal-velocity events

(normal- $v_{\text{Si II}}$ SNe Ia; defined as $v_{\text{Si II}} < 12,000 \text{ km s}^{-1}$) span a wider range of radial distance. Given the metallicity gradients observed in both the Milky Way and many external galaxies (e.g., Henry & Worthey 1999), they suggested the metallicity could be important in driving this relation. Pan et al. (2015, hereafter P15) further supported this idea by finding some evidence that high- $v_{\text{Si II}}$ SNe Ia tend to reside in more massive galaxies than the normal- $v_{\text{Si II}}$ counterparts, although their results are not statistically significant due to the small sample size. These host studies together suggested there could be at least two distinct populations of SNe Ia in terms of their ejecta velocities.

High- $v_{\text{Si II}}$ SN Ia has long been suspected to have a different origin from normal- $v_{\text{Si II}}$ SN Ia. This was firstly proposed by Wang et al. (2009), where they found high- $v_{\text{Si II}}$ SNe Ia tend to be redder and prefer a lower extinction ratio (R_V) than normal- $v_{\text{Si II}}$ SNe Ia. Foley & Kasen (2011) argued the high- $v_{\text{Si II}}$ SNe Ia actually do not have a different reddening law but are intrinsically redder than normal- $v_{\text{Si II}}$ SNe Ia. Recently, Wang et al. (2019) found some evidence that these high- $v_{\text{Si II}}$ SNe Ia tend to show blue excess in their late-time light-curves and variable Na I absorption lines in their spectra. These observations were attributed as the circumstellar dust surrounding the SNe. They claimed the high- $v_{\text{Si II}}$ SNe Ia are likely associated with the single degenerate systems.

Theoretical study also suggested the high- $v_{\text{Si II}}$ SNe Ia may originate from unique explosions. Using 1D WD explosion models, Polin et al. (2019) showed the sub-Chandrasekhar explosions could produce SNe Ia with a wide range of $v_{\text{Si II}}$. Their results further indicated the high- $v_{\text{Si II}}$ SNe Ia could be primarily produced by sub-Chandrasekhar type of explosions. The red color found for high- $v_{\text{Si II}}$ SNe Ia can also be explained by the line blanketing effect due the ashes of helium shell in their models.

In this paper, we revisit the relation between SN Ia

¹ Division of Science, National Astronomical Observatory of Japan, 2-21-1 Osawa, Mitaka, Tokyo 181-8588, Japan

² EACOA Fellow

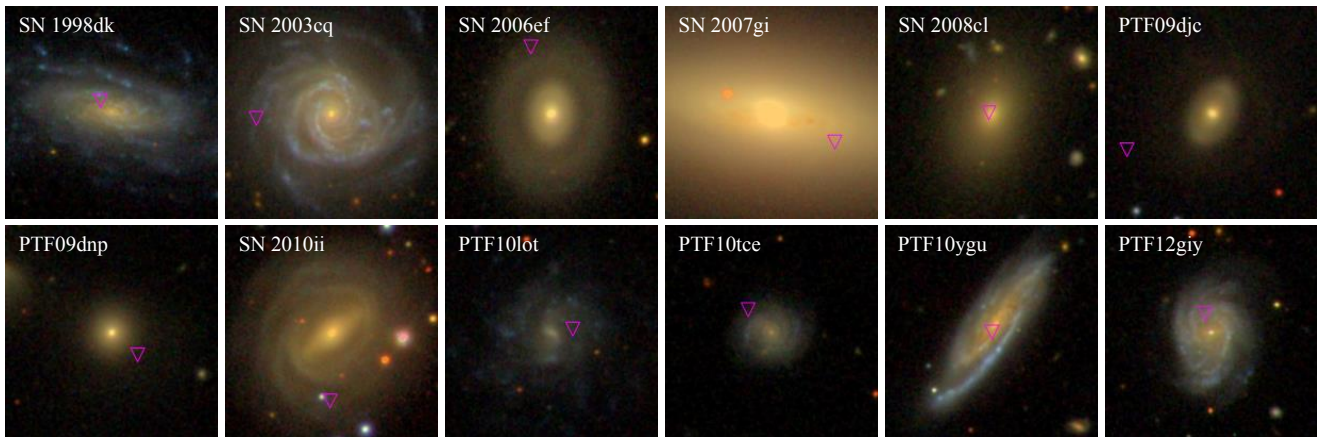


FIG. 1.— Some examples of high $\text{Si II } \lambda 6355$ velocity SN Ia (high- $v_{\text{Si II}}$ SN Ia; defined as $v_{\text{Si II}} \geq 12000 \text{ km s}^{-1}$) host galaxies in this work. The position of the SN is indicated by the purple triangle. Images are all generated from SDSS with a size of $80'' \times 80''$. North is up and east is left.

$v_{\text{Si II}}$ and host-galaxy properties with a parent sample of ~ 280 SNe Ia ($\gtrsim 2$ times larger than that in P15), with the purpose to differentiate the progenitor properties and explosion mechanisms between high- $v_{\text{Si II}}$ and normal- $v_{\text{Si II}}$ SNe Ia. A plan of the paper follows. In Section 2 we introduce our SN Ia spectral sample and the determination of host parameters. We show the results in Section 3. The discussion and conclusions are presented in Section 4 and Section 5, respectively. Throughout this paper, we assume $H_0 = 70 \text{ km s}^{-1} \text{ Mpc}^{-1}$ and a flat universe with $\Omega_M = 0.3$.

2. DATA AND METHOD

2.1. SN data

In this work, we extend our analysis with the full spectroscopic sample studied in Maguire et al. (2014, hereafter M14). This is the parent sample of what was studied by P15, containing 264 spectroscopically normal SNe Ia with $\text{Si II } \lambda 6355$ measurements near peak (e.g., within 5 days from the peak luminosity). They were all discovered by the Palomar Transient Factory (PTF). In addition to the PTF sample, we further include the SNe studied in Silverman et al. (2015, hereafter S15) to increase our sample size. This added another ~ 150 SNe Ia with near-peak $\text{Si II } \lambda 6355$ measurements from the Berkeley SN Ia Program (BSNIP) after removing the duplicate objects from our PTF sample. This gives a sample of ~ 400 SNe Ia at $z < 0.2$. The description of the spectroscopic observation and data reduction can be found in detail in M14 and S15.

Since M14 and S15 used very similar techniques in measuring the spectral features, we do not perform new measurements but simply adopting their results in our analysis. A complete description of the line measurement can be found in M14. Briefly speaking, the SN spectrum is firstly corrected into the rest frame, define (by eye inspection) continuum regions on either side of the feature, and fit a straight line pseudo-continuum across the absorption feature. The feature is then normalised by dividing it by the pseudo-continuum. A Gaussian fit is performed to the normalised $\text{Si II } \lambda 6355$ line in velocity space. The resulting fit then gives the velocity and pseudo-equivalent widths (pEW) of the feature.

2.2. Host-galaxy properties

The main purpose of this work is to investigate the relation between $v_{\text{Si II}}$ of SNe Ia and their host properties. The host stellar mass (M_{stellar}) is derived by fitting the photometry of the host galaxy with the photometric redshift code Z-PEG (Le Borgne & Rocca-Volmerange 2002). The host photometry is provided from SDSS *ugriz* catalog (Abolfathi et al. 2018). The SDSS model magnitudes are used here. Z-PEG fits the observed galaxy colours with galaxy spectral energy distribution (SED) templates corresponding to 9 spectral types (SB, Im, Sd, Sc, Sbc, Sb, Sa, S0, and E). Here we assume a Salpeter (1955) initial-mass function (IMF). The photometry is corrected for foreground Milky Way reddening with $R_V = 3.1$ and a Cardelli, Clayton, & Mathis (1989, CCM) reddening law. Fig. 1 shows some SDSS color images of high- $v_{\text{Si II}}$ SN Ia host galaxies studied in this work.

We also measure the host gas-phase metallicity and star-formation rate (SFR). This is done by obtaining the optical spectra of the host galaxies, primarily with the SDSS spectrograph on the Sloan Foundation 2.5-m telescope and Gemini Multi-Object Spectrographs (GMOS) on the Gemini Observatory. We fit the emission lines and stellar continuum of the host spectrum using the Interactive Data Language (IDL) codes PPXF (Cappellari & Emsellem 2004) and GANDALF (Sarzi et al. 2006). A complete description of this process can be found in Pan et al. (2014). Briefly, PPXF fits the line-of-sight velocity distribution (LOSVD) of the stars in the galaxy in pixel space using a series of stellar templates. Before fitting the stellar continuum, the wavelengths of potential emission lines are masked to remove any possible contamination. The stellar templates are based on the MILES empirical stellar library (Sánchez-Blázquez et al. 2006; Vazdekis et al. 2010). A total of 288 templates is selected with $[M/H] = -1.71$ to $+0.22$ in 6 bins and ages ranging from 0.063 to 14.12 Gyr in 48 bins.

We correct all spectra for foreground Galactic reddening using the calibrations of Schlafly & Finkbeiner (2011). The host-galaxy extinction is corrected with the two-component reddening model in GANDALF. The first component assumes a diffusive dust throughout the whole galaxy that affects the entire spectrum. It is determined by comparing the observed spectra to the un-reddened spectral templates. The second component measures the local dust around the nebular regions and

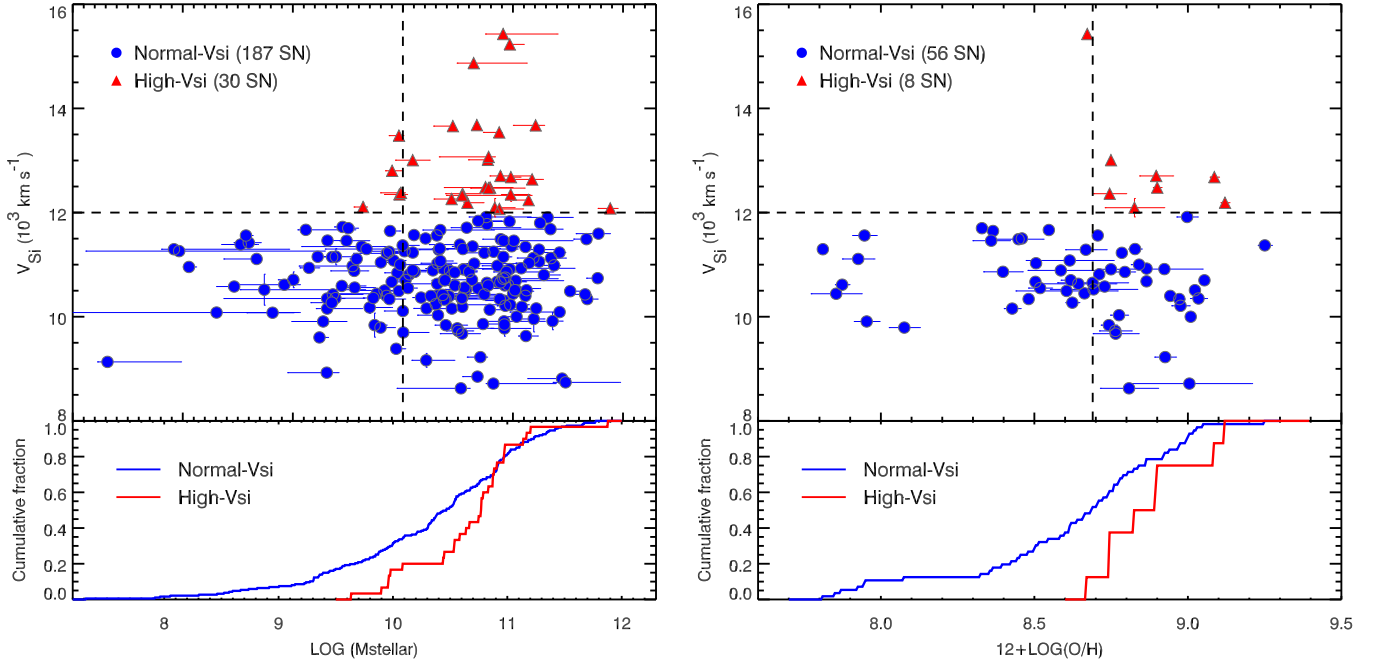


FIG. 2.— *Left:* The Si II $\lambda 6355$ velocities ($v_{\text{Si II}}$) as a function of host-galaxy stellar mass (M_{stellar}). The high- $v_{\text{Si II}}$ SNe Ia are shown as red triangles, and the normal- $v_{\text{Si II}}$ SNe Ia are shown as blue circles. The vertical and horizontal dashed lines represent the criterion used to split the sample in velocity and M_{stellar} space, respectively. The bottom histograms show the cumulative fractions of M_{stellar} for high- $v_{\text{Si II}}$ and normal- $v_{\text{Si II}}$ SNe Ia. *Right:* The same as left panel, but with host-galaxy gas-phase metallicity instead.

affects only the emission lines. It is constrained only if the Balmer decrement (the $\text{H}\alpha$ to $\text{H}\beta$ line ratio) can be measured.

After the emission-line measurements from PPXF and GANDALF, we determine the SFR by adopting the conversion of Kennicutt (1998), which used evolutionary synthesis models to relate the luminosity of the $\text{H}\alpha$ line to the SFR. We calculate the host gas-phase metallicity based on the diagnostics from Dopita et al. (2016). Dopita et al. (2016) used the ratios of $[\text{N II}] \lambda 6584$ to $[\text{S II}] \lambda \lambda 6717, 6731$ and $[\text{N II}] \lambda 6584$ to $\text{H}\alpha$ to calibrate the gas-phase metallicity. This has the advantage of requiring a narrow wavelength range and therefore is less affected by the reddening correction. We further use BPT diagrams (Baldwin, Phillips, & Terlevich 1981) to check for potential contamination from active galactic nuclei (AGNs) in our host galaxies. The criteria proposed by Kewley et al. (2001) are adopted to distinguish between normal and AGN host galaxies. The potential AGNs are excluded from our emission line analyses. A summary of our measurements can be found in Table 1.

3. ANALYSIS

We firstly investigate the relation between $v_{\text{Si II}}$ and host M_{stellar} . Ideally, one should distinguish between high- $v_{\text{Si II}}$ and normal- $v_{\text{Si II}}$ SNe Ia with the $v_{\text{Si II}}$ measured exactly at peak luminosity. In practice, previous studies generally used the spectra within a few days from the peak given that the spectral evolution is relatively mild at those epochs. M14 measured $v_{\text{Si II}}$ using all the spectra observed within 5 days from the peak luminosity and did not apply phase corrections to their line measurements. Given a larger sample size, we adopt a more stringent phase criterion in this work; we use all the spectra observed within only 3 days from the peak luminosity. That way the $v_{\text{Si II}}$ of different SNe are compared

at closer phases and reduces the uncertainties of phase evolution. This gives a final parent sample of 281 SNe (41 of them are high- $v_{\text{Si II}}$ SNe Ia), which is still more than 2 times larger than that studied in P15. Releasing this criterion does not change our conclusion but only making our results less significant.

The result is shown in the left panel of Fig. 2. We find clear evidence that most of the high- $v_{\text{Si II}}$ SNe Ia reside in massive galaxies ($\log(M_{\text{stellar}}) > 10 M_{\odot}$), whereas the normal- $v_{\text{Si II}}$ SNe Ia can be found in both lower-mass and massive galaxies. This is consistent with the finding in P15. Here we confirm this trend with a much larger sample and our results are statistically more significant. Both Kolmogorov-Smirnov (K-S) and Anderson-Darling (A-D) tests give a p -value of $\lesssim 0.02$ that the M_{stellar} distributions of high- $v_{\text{Si II}}$ and normal- $v_{\text{Si II}}$ SNe Ia are drawn from the same underlying population. This value is ~ 10 times smaller than that studied in P15. It is also evident that this relation is neither linear nor monotonic. In fact, it implies the existence of multiple populations of SNe Ia (see Section 4.1 for a discussion).

We also note the $v_{\text{Si II}}$ of $\sim 12000 \text{ km s}^{-1}$ is a fairly good criterion to distinguish between high- $v_{\text{Si II}}$ and normal- $v_{\text{Si II}}$ SNe Ia. For SNe with $v_{\text{Si II}} > 12000 \text{ km s}^{-1}$, ~ 84 percent of their host galaxies have $\log(M_{\text{stellar}}) > 10 M_{\odot}$. The ratio goes up to only ~ 90 percent if the criterion is raised to 13000 km s^{-1} , but drops significantly to ~ 68 percent if the criterion is lowered to 11000 km s^{-1} . All of the SNe with $v_{\text{Si II}} > 12000 \text{ km s}^{-1}$ have $\log(M_{\text{stellar}}) > 9.6 M_{\odot}$.

Next we investigate the relation with host gas-phase metallicity. The result is shown in the right panel of Fig. 2. Given the tight relation between M_{stellar} and metallicity (e.g., Tremonti et al. 2004), it is reasonable to suspect that the metallicity is the underlying source to drive the relation we see with M_{stellar} . In general, we find

the relation between $v_{\text{Si II}}$ and host metallicity is consistent with what we have found for host M_{stellar} . The host galaxies of high- $v_{\text{Si II}}$ SNe Ia tend to be metal-rich, having metallicities mostly above solar value (8.69; Allende Prieto et al. 2001). The K-S and A-D tests give a p -value of 0.05 and 0.04, respectively, that the metallicity distributions of high- $v_{\text{Si II}}$ and normal- $v_{\text{Si II}}$ SNe Ia are drawn from the same underlying population. This is less significant than the trend with host M_{stellar} . However, our sample with host metallicity measurements is only one third the size of that with host M_{stellar} . The progenitor metallicity is also expected to differ from nuclear metallicity measurements performed in this work. A larger sample with direct metallicity measurements near the SN location is critical to constrain the metallicity effect in the future.

4. DISCUSSION

4.1. Silicon velocity and metallicity

Lentz et al. (2000) showed that the observed $v_{\text{Si II}}$ could vary with the C+O layer metallicity in SN Ia. The blue-shifted velocity of the Si II $\lambda 6355$ feature increase with C+O layer metallicity due to the increasing opacity in the C+O layer moving the features blueward and causing larger line velocities. P15 determined a linear relation between the $v_{\text{Si II}}$ and C+O metallicity of SN progenitor using the models of Lentz et al. (2000) and showed the $v_{\text{Si II}}$ increase with metallicities with a slope of $435 \text{ km s}^{-1} \text{ dex}^{-1}$. They claimed the observed relation between host M_{stellar} and $v_{\text{Si II}}$ is in qualitative agreement with that of Lentz et al. (2000) models. However, fitting a linear relation between the observed $v_{\text{Si II}}$ and host gas-phase metallicity with our sample (i.e., right panel of Fig. 2) gives a slope of $87 \pm 427 \text{ km s}^{-1} \text{ dex}^{-1}$, which is consistent with no trend.

In fact, it is now evident that both high- $v_{\text{Si II}}$ and normal- $v_{\text{Si II}}$ SNe Ia can be found in metal-rich host environments. If the high photospheric velocity is mainly caused by the increasing opacity (due to higher progenitor metallicity) in SN, we would expect a monotonic relation between $v_{\text{Si II}}$ and host metallicity, instead of a L-shaped distribution shown in both panels of Fig. 2. Thus, it is not precise to say that the high- $v_{\text{Si II}}$ SNe Ia tend to reside in *more* metal-rich environments than that of normal- $v_{\text{Si II}}$ SNe Ia. While the opacity could still have some effect here, we argue that there are likely at least two populations of SNe Ia responsible for the observed trend. The high- $v_{\text{Si II}}$ SNe Ia could be part of a unique population which is sensitive to the progenitor metallicity and can only be formed in metal-rich environments (see Section 4.2 for a discussion).

4.2. Implications on progenitor systems and explosion mechanisms

Wang et al. (2013) found high- $v_{\text{Si II}}$ SNe Ia are more concentrated in the inner and brighter regions of their host galaxies. They suggested the high- $v_{\text{Si II}}$ SNe Ia likely originate from younger and more metal-rich progenitors than those of normal- $v_{\text{Si II}}$ SNe Ia. Recently, Wang et al. (2019) showed some evidence that these high- $v_{\text{Si II}}$ SNe Ia tend to present blue excess in their late-time light-curves and variable Na I absorption lines in the spectra. They attributed these observations to the circumstellar dust

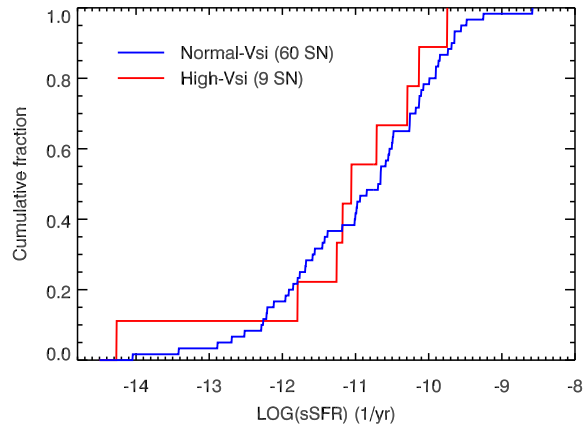


FIG. 3.— The cumulative fractions of specific star-formation rate (sSFR) for high- $v_{\text{Si II}}$ (red) and normal- $v_{\text{Si II}}$ (blue) SNe Ia.

surrounding the SNe and concluded that the high- $v_{\text{Si II}}$ and normal- $v_{\text{Si II}}$ SNe Ia are likely from the single degenerate and double degenerate systems, respectively.

Our results support that the high- $v_{\text{Si II}}$ SN Ia has a strong preference to occur in metal-rich environment. However, we argue that they may not come from particularly young populations. Fig. 3 shows the cumulative fractions of specific star-formation rate (sSFR) for high- $v_{\text{Si II}}$ and normal- $v_{\text{Si II}}$ SNe Ia. Here the sSFR is defined as the SFR per unit M_{stellar} . Theoretically, the sSFR is a more appropriate indicator to measure the relative star-formation activity of a galaxy as it measures the star-formation relative to the underlying galaxy stellar mass (Guzman et al. 1997). There is also a strong correlation between sSFR and age of the galaxies, in a sense that higher-sSFR galaxies tend to have younger stellar populations than lower-sSFR galaxies (e.g., Brinchmann et al. 2004).

We find the difference between high- $v_{\text{Si II}}$ and normal- $v_{\text{Si II}}$ SNe Ia is not statistically significant in terms of their host sSFR. The K-S test gives a p -value of 0.93 that the sSFR distributions of high- $v_{\text{Si II}}$ and normal- $v_{\text{Si II}}$ SNe Ia are drawn from the same underlying population. We determine a mean $\log(\text{sSFR})$ of $-10.93 \pm 1.11 \text{ yr}^{-1}$ and $-11.15 \pm 1.16 \text{ yr}^{-1}$ for normal- $v_{\text{Si II}}$ and high- $v_{\text{Si II}}$ SNe Ia, respectively. Thus, the host galaxies of high- $v_{\text{Si II}}$ SNe Ia do not tend to be younger than their normal- $v_{\text{Si II}}$ counterparts. This is consistent with the results in P15, where they showed the youngest populations are likely related to those SNe Ia with dispatched high-velocity features (HVF), not those with high photospheric velocities. They also found there is a significant number (more than 30 percent) of high- $v_{\text{Si II}}$ SNe Ia in early-type galaxies. Our results imply the metallicity is probably the only important (or dominant) factor in forming high- $v_{\text{Si II}}$ SNe Ia.

Theoretical studies also suggested the high- $v_{\text{Si II}}$ SNe Ia may have unique explosion mechanisms. Using 1D WD explosion models, Polin et al. (2019) showed the sub-Chandrasekhar class of explosions can produce SNe Ia of a wide range of luminosities and photospheric velocities. In particular, their results indicated the high- $v_{\text{Si II}}$ SNe Ia could be primarily produced by sub-Chandrasekhar explosions, whereas normal- $v_{\text{Si II}}$ SNe Ia can be produced by both sub-Chandrasekhar and near-Chandrasekhar explosions. The significant line blanketing due to the ashes

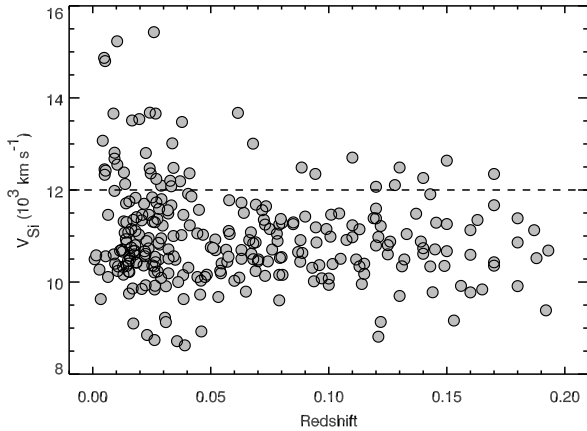


FIG. 4.— The Si II $\lambda 6355$ velocities ($v_{\text{Si II}}$) as a function of redshift. The dashed line represents the criterion used to split the high- $v_{\text{Si II}}$ and normal- $v_{\text{Si II}}$ SNe Ia (i.e., $v_{\text{Si II}} = 12000 \text{ km s}^{-1}$).

of helium shell in their models also explained the intrinsically red color of high- $v_{\text{Si II}}$ SNe Ia (e.g., Foley & Kasen 2011). However, it is not yet clear the contribution of progenitor metallicity on such models.

Progenitor metallicity is believed to have significant impact on explosions of SN Ia. For example, it may affect the accretion onto the WD by changing the opacity in the wind for some single degenerate scenarios (e.g., Kobayashi et al. 1998). The mass of the WD is also expected to vary with metallicity. At a given mass, stars of higher metallicity generally produce less massive WDs (e.g., Umeda et al. 1999). This implies they may be more difficult to reach the Chandrasekhar limit for explosions. Under the circumstances, the sub-Chandrasekhar class of explosions are probably more efficient and may account for some SNe Ia having higher progenitor metallicities. The preference of metal-rich environments can be used as a strong constraint to discriminate between models for high- $v_{\text{Si II}}$ SNe Ia in the future.

4.3. Implications on cosmology

Our results also have significant implications on cosmology. Foley & Kasen (2011) found high- $v_{\text{Si II}}$ SNe Ia are intrinsically redder (in terms of $B - V$ at maximum light) than normal- $v_{\text{Si II}}$ SNe Ia. By accounting for this color difference, they reduced the scatter in Hubble residuals (HRs). Also recently, Siebert et al. (2020) determined a $\sim 3\text{-}\sigma$ HR step between high- $v_{\text{Si II}}$ and normal- $v_{\text{Si II}}$ SNe Ia, with high- $v_{\text{Si II}}$ SNe Ia having more negative HRs than the normal- $v_{\text{Si II}}$ SNe Ia. These results are indicative that the ejecta velocity can be used to improve SN Ia distances.

Moreover, if the fraction of high- $v_{\text{Si II}}$ to normal- $v_{\text{Si II}}$ SNe Ia changes with redshift, it could introduce significant bias on our cosmological analysis when assuming a single intrinsic color for SN Ia (Foley & Kasen 2011). Given the strong preference of metal-rich environments for high- $v_{\text{Si II}}$ SNe Ia, we would expect an evolution on the number of discovered high- $v_{\text{Si II}}$ SNe Ia with redshift, with a decreased rate towards higher redshifts. Fig. 4 shows the $v_{\text{Si II}}$ as the function of redshift with our sample. We find some evidence that the ratio of high- $v_{\text{Si II}}$ to normal- $v_{\text{Si II}}$ SNe Ia tend to be higher at lower redshifts. At $z < 0.1$, ~ 16 percent (13 percent if using untargeted PTF sample only) of SNe in our sample are high- $v_{\text{Si II}}$

SNe, while only ~ 11 percent of the SNe are high- $v_{\text{Si II}}$ SNe at $z > 0.1$. It is also obvious that the extremely high- $v_{\text{Si II}}$ SNe Ia (e.g., $v_{\text{Si II}} \gtrsim 13000 \text{ km s}^{-1}$) are hardly found at $z > 0.1$.

However, the selection effect might play a role for SNe discovered at $z > 0.1$ in our sample (for a discussion, see Pan et al. 2014). For example, we would expect a bias if the high- $v_{\text{Si II}}$ SNe Ia are significantly brighter or fainter than normal- $v_{\text{Si II}}$ SNe Ia. Using $\Delta m_{15}(B)$ as the proxy of SN Ia brightness, we determine a mean $\Delta m_{15}(B)$ of $1.12 \pm 0.33 \text{ mag}$ and $1.12 \pm 0.22 \text{ mag}$ for normal- $v_{\text{Si II}}$ and high- $v_{\text{Si II}}$ SNe Ia, respectively. This indicates (on average) they are not different in brightness. Thus, there is unlikely a Malmquist bias (at least) on the fraction of high- $v_{\text{Si II}}$ to normal- $v_{\text{Si II}}$ SNe Ia at higher redshifts. We also note that the high- $v_{\text{Si II}}$ SNe Ia tend to show less dispersion in $\Delta m_{15}(B)$ than that of normal- $v_{\text{Si II}}$ SNe Ia. It is unclear if this trend is intrinsic to the explosion or simply due to the smaller sample size of high- $v_{\text{Si II}}$ SNe Ia.

Another caveat is the difficulty in finding SNe on very bright galaxy backgrounds, where the contrast of the SN over the host galaxy is low. Since high- $v_{\text{Si II}}$ SNe Ia tend to be found in massive galaxies and are more concentrated in the inner regions of their hosts, they may be more difficult to be found at higher redshifts. However, this is only an issue with modern image subtraction techniques when the SN brightness drops to $< 10\%$ of that of the host background (e.g., Perrett et al. 2010). The future analysis with data taken from higher-redshift surveys (e.g., Pan-STARRS1; Pan et al., in preparation) will be necessary to constrain the potential evolution of high- $v_{\text{Si II}}$ SNe Ia.

5. CONCLUSIONS

In this work, we investigate the relation between photospheric Si II $\lambda 6355$ velocities ($v_{\text{Si II}}$) and host-galaxy properties of SN Ia. A more stringent criterion on the phase of SN spectra is adopted to distinguish between normal- $v_{\text{Si II}}$ and high- $v_{\text{Si II}}$ SNe Ia. We find the high- $v_{\text{Si II}}$ SNe Ia are likely formed from a distinct population which favors massive host environments. This is further supported by the direct measurements on host gas-phase metallicities. Although opacity may have some effect (due to progenitor metallicity), we argue the difference in photospheric velocities between high- $v_{\text{Si II}}$ and normal- $v_{\text{Si II}}$ SNe Ia is mainly caused by different explosion mechanisms.

Theoretical studies suggested the high- $v_{\text{Si II}}$ SNe Ia may originate from sub-Chandrasekhar explosions. This is consistent with our results. At a given mass, stars of higher metallicities generally produce less massive WDs. This may increase the chance for them to explode under sub-Chandrasekhar mass. Nevertheless, the detailed investigation is still needed to evaluate the effect of progenitor metallicity on such models.

Previous studies also suggested the high- $v_{\text{Si II}}$ and normal- $v_{\text{Si II}}$ SNe Ia could be formed via single degenerate and double degenerate scenarios, respectively. However, we find high- $v_{\text{Si II}}$ SNe Ia do not tend to originate from younger populations than that of normal- $v_{\text{Si II}}$ SNe Ia. We argue the metallicity is the only important factor in forming high- $v_{\text{Si II}}$ SNe Ia.

Our results also imply potential evolution of high- $v_{\text{Si II}}$ SNe Ia. We would expect less high- $v_{\text{Si II}}$ SNe Ia to be discovered at higher redshifts when the Universe is more

metal-poor than present. This evolution could introduce a bias on our cosmological analysis given that high- $v_{\text{Si II}}$ and normal- $v_{\text{Si II}}$ SNe Ia tend to have intrinsically different colors. Future spectroscopic studies using higher-redshift dataset will be critical to measure this evolution

effect.

ACKNOWLEDGMENTS

Y.-C.P. is supported by the East Asian Core Observatories Association (EACOA) Fellowship.

REFERENCES

- Abolfathi, B., Aguado, D. S., Aguilar, G., et al. 2018, *ApJS*, 235, 42
- Allende Prieto, C., Lambert, D. L., & Asplund, M. 2001, *ApJ*, 556, L63
- Baldwin, J. A., Phillips, M. M., & Terlevich, R. 1981, *PASP*, 93, 5
- Bloom, J. S., Kasen, D., Shen, K. J., et al. 2012, *ApJ*, 744, L17
- Brinchmann, J., Charlot, S., White, S. D. M., et al. 2004, *MNRAS*, 351, 1151
- Cappellari, M., & Emsellem, E. 2004, *PASP*, 116, 138
- Cardelli, J. A., Clayton, G. C., & Mathis, J. S. 1989, *ApJ*, 345, 245
- Childress, M., Aldering, G., Antilogus, P., et al. 2013, *ApJ*, 770, 108
- D’Andrea, C. B., Gupta, R. R., Sako, M., et al. 2011, *ApJ*, 743, 172
- Dopita, M. A., Kewley, L. J., Sutherland, R. S., & Nicholls, D. C. 2016, *Ap&SS*, 361, 61
- Foley, R. J., & Kasen, D. 2011, *ApJ*, 729, 55
- Guzman, R., Gallego, J., Koo, D. C., et al. 1997, *ApJ*, 489, 559
- Henry, R. B. C., & Worthey, G. 1999, *PASP*, 111, 919
- Hillebrandt, W., Kromer, M., Röpke, F. K., & Ruiter, A. J. 2013, *Frontiers of Physics*, 8, 116
- Hillebrandt, W., & Niemeyer, J. C. 2000, *ARA&A*, 38, 191
- Iben, Jr., I., & Tutukov, A. V. 1984, *ApJS*, 54, 335
- Johansson, J., Thomas, D., Pforr, J., et al. 2013, *MNRAS*, 435, 1680
- Kelly, P. L., Hicken, M., Burke, D. L., Mandel, K. S., & Kirshner, R. P. 2010, *ApJ*, 715, 743
- Kennicutt, J. R. C. 1998, *ARA&A*, 36, 189
- Kewley, L. J., Dopita, M. A., Sutherland, R. S., Heisler, C. A., & Trevena, J. 2001, *ApJ*, 556, 121
- Kobayashi, C., Tsujimoto, T., Nomoto, K., Hachisu, I., & Kato, M. 1998, *ApJ*, 503, L155
- Lampeitl, H., Smith, M., Nichol, R. C., et al. 2010, *ApJ*, 722, 566
- Le Borgne, D., & Rocca-Volmerange, B. 2002, *A&A*, 386, 446
- Lentz, E. J., Baron, E., Branch, D., Hauschildt, P. H., & Nugent, P. E. 2000, *ApJ*, 530, 966
- Maguire, K., Sullivan, M., Pan, Y. C., et al. 2014, *MNRAS*, 444, 3258
- Maoz, D., Mannucci, F., & Nelemans, G. 2014, *ARA&A*, 52, 107
- Nugent, P. E., Sullivan, M., Cenko, S. B., et al. 2011, *Nature*, 480, 344
- Pan, Y. C., Sullivan, M., Maguire, K., et al. 2015, *MNRAS*, 446, 354
- Pan, Y.-C., Sullivan, M., Maguire, K., et al. 2014, *MNRAS*, 438, 1391
- Perrett, K., Balam, D., Sullivan, M., et al. 2010, *AJ*, 140, 518
- Polin, A., Nugent, P., & Kasen, D. 2019, *ApJ*, 873, 84
- Salpeter, E. E. 1955, *ApJ*, 121, 161
- Sánchez-Blázquez, P., Peletier, R. F., Jiménez-Vicente, J., et al. 2006, *MNRAS*, 371, 703
- Sarzi, M., Falcón-Barroso, J., Davies, R. L., et al. 2006, *MNRAS*, 366, 1151
- Schlafly, E. F., & Finkbeiner, D. P. 2011, *ApJ*, 737, 103
- Siebert, M. R., Foley, R. J., Jones, D. O., & Davis, K. W. 2020, *MNRAS*, arXiv:2002.09490
- Silverman, J. M., Vinkó, J., Marion, G. H., et al. 2015, *MNRAS*, 451, 1973
- Sullivan, M., Conley, A., Howell, D. A., et al. 2010, *MNRAS*, 406, 782
- Tremonti, C. A., Heckman, T. M., Kauffmann, G., et al. 2004, *ApJ*, 613, 898
- Umeda, H., Nomoto, K., Yamaoka, H., & Wanajo, S. 1999, *ApJ*, 513, 861
- Vazdekis, A., Sánchez-Blázquez, P., Falcón-Barroso, J., et al. 2010, *MNRAS*, 404, 1639
- Wang, X., Chen, J., Wang, L., et al. 2019, *ApJ*, 882, 120
- Wang, X., Wang, L., Filippenko, A. V., Zhang, T., & Zhao, X. 2013, *Science*, 340, 170
- Wang, X., Filippenko, A. V., Ganeshalingam, M., et al. 2009, *ApJ*, 699, L139
- Webbink, R. F. 1984, *ApJ*, 277, 355
- Whelan, J., & Iben, Jr., I. 1973, *ApJ*, 186, 1007

TABLE 1
SUMMARY OF OUR SAMPLE IN THIS WORK.

SN Name	Redshift	$v_{\text{Si II}}$ (km s^{-1})	$\log M_{\text{stellar}}$ (M_{\odot})	$12 + \log (\text{O}/\text{H})$
PTF09bai	0.180	11385 ± 18	$10.518^{+0.104}_{-0.279}$...
PTF09bj	0.144	9777 ± 50	$10.495^{+0.324}_{-0.123}$...
PTF09dj	0.034	13013 ± 16	$10.771^{+0.008}_{-0.176}$...
PTF09dlc	0.067	10615 ± 9	$8.923^{+0.138}_{-0.433}$	7.874 ± 0.023
PTF09dnl	0.024	10955 ± 4	$8.056^{+0.062}_{-0.053}$...
PTF09dnp	0.037	12189 ± 7	$10.586^{+0.143}_{-0.033}$	9.121 ± 0.013
PTF09dqt	0.113	11146 ± 22	$9.357^{+0.055}_{-0.011}$...
PTF09dxo	0.052	10924 ± 10	$10.364^{+0.449}_{-0.157}$	8.865 ± 0.014
PTF09e	0.149	10349 ± 38	$9.312^{+0.154}_{-0.939}$...
PTF09fox	0.072	11560 ± 11	$10.309^{+0.033}_{-0.034}$	8.706 ± 0.005
PTF09foz	0.054	10190 ± 8	$10.540^{+0.039}_{-0.147}$...
PTF09gn	0.139	10880 ± 72	$9.558^{+0.124}_{-0.215}$...
PTF09gul	0.072	11352 ± 33	$10.988^{+0.145}_{-0.011}$...
PTF09h	0.121	10979 ± 31	$10.859^{+0.074}_{-0.140}$...
PTF09ib	0.122	11216 ± 15	$9.854^{+0.177}_{-0.303}$...
PTF09isn	0.101	11463 ± 37	$9.315^{+0.128}_{-0.015}$...
PTF09s	0.046	8926 ± 14	$9.308^{+0.104}_{-0.355}$...
PTF09v	0.119	11386 ± 37	$8.526^{+0.154}_{-0.173}$...
PTF10aaea	0.160	9775 ± 147	$10.923^{+0.232}_{-0.125}$...
PTF10abjv	0.076	10705 ± 27	$10.024^{+0.039}_{-0.079}$...
PTF10acqp	0.170	12347 ± 132	$10.980^{+0.167}_{-0.085}$...
PTF10bhw	0.110	11233 ± 25	$11.423^{+0.049}_{-0.239}$...
PTF10cmj	0.112	10490 ± 30	$11.117^{+0.064}_{-0.057}$...
PTF10cwm	0.079	10525 ± 18	$10.575^{+0.072}_{-0.194}$	8.693 ± 0.141
PTF10cxk	0.018	10938 ± 13	$9.147^{+0.090}_{-0.083}$...
PTF10duy	0.079	9602 ± 15	$9.242^{+0.074}_{-0.047}$...
PTF10duz	0.064	11502 ± 33	$10.206^{+0.111}_{-0.044}$	8.459 ± 0.010
PTF10fej	0.110	12703 ± 82	$10.886^{+0.270}_{-0.096}$	8.897 ± 0.054
PTF10fj	0.050	10757 ± 19	$10.906^{+0.137}_{-0.009}$...
PTF10fxe	0.099	11152 ± 155	$9.391^{+0.206}_{-0.149}$...
PTF10fxl	0.030	11227 ± 12	$10.740^{+0.013}_{-0.165}$	8.785 ± 0.003
PTF10fxp	0.104	11490 ± 17	$11.668^{+0.039}_{-0.117}$...
PTF10fxq	0.107	10914 ± 34	$10.971^{+0.079}_{-0.249}$	8.923 ± 0.123
PTF10fyl	0.055	10405 ± 9	$10.312^{+0.004}_{-0.180}$...
PTF10glo	0.075	11151 ± 31	$9.226^{+0.083}_{-0.029}$...
PTF10gnj	0.078	10889 ± 19	$10.273^{+0.098}_{-0.120}$	8.586 ± 0.107
PTF10goo	0.087	10651 ± 31	$10.763^{+0.106}_{-0.210}$	8.690 ± 0.114
PTF10gop	0.097	10080 ± 33	$8.307^{+0.753}_{-1.440}$...
PTF10goq	0.088	10910 ± 59	$10.557^{+0.086}_{-0.215}$...
PTF10hdm	0.165	9839 ± 230	$9.743^{+0.106}_{-0.030}$...
PTF10hld	0.038	13477 ± 24	$9.964^{+0.037}_{-0.090}$...
PTF10jab	0.187	11126 ± 16	$11.346^{+0.132}_{-0.014}$...
PTF10lot	0.022	12802 ± 16	$9.902^{+0.079}_{-0.061}$...
PTF10mtd	0.079	11248 ± 15	$9.875^{+0.101}_{-0.065}$...
PTF10mwb	0.031	9909 ± 4	$9.276^{+0.208}_{-0.286}$	7.954 ± 0.041
PTF10ncy	0.130	9697 ± 45	$10.003^{+0.226}_{-0.031}$...
PTF10ncz	0.170	10429 ± 95	$9.364^{+0.266}_{-0.025}$...
PTF10nda	0.101	10985 ± 26	$11.374^{+0.049}_{-0.216}$...
PTF10nhu	0.153	9163 ± 132	$10.212^{+0.252}_{-0.131}$...
PTF10nnh	0.150	10670 ± 106	$10.856^{+0.261}_{-0.065}$...
PTF10nvh	0.068	10843 ± 8	$9.950^{+0.071}_{-0.117}$...
PTF10oth	0.145	11289 ± 35	$11.237^{+0.174}_{-0.103}$...
PTF10pvh	0.105	10504 ± 39	$9.833^{+0.179}_{-0.247}$...
PTF10pvi	0.080	11286 ± 46	$10.326^{+0.079}_{-0.178}$	8.668 ± 0.066
PTF10qhp	0.032	11488 ± 25	$10.889^{+0.025}_{-0.165}$	8.448 ± 0.080
PTF10qjl	0.058	11109 ± 5	$8.671^{+0.020}_{-0.299}$	7.926 ± 0.052
PTF10qjq	0.028	10813 ± 12	$10.059^{+0.087}_{-0.044}$	8.711 ± 0.003

TABLE 2
SUMMARY OF OUR SAMPLE IN THIS WORK (CONTINUED).

SN Name	Redshift	$v_{\text{Si II}}$ (km s^{-1})	$\log M_{\text{stellar}}$ (M_{\odot})	$12 + \log (\text{O}/\text{H})$
PTF10qkf	0.080	10156 ± 55	$10.445^{+0.115}_{-0.161}$	8.428 ± 0.026
PTF10qky	0.074	10448 ± 13	$10.559^{+0.094}_{-0.116}$	8.663 ± 0.005
PTF10qny	0.033	11664 ± 12	$10.340^{+0.484}_{-0.160}$	8.547 ± 0.014
PTF10qsc	0.088	10441 ± 31	$9.762^{+0.137}_{-0.378}$	7.854 ± 0.082
PTF10qwg	0.068	13006 ± 16	$10.089^{+0.151}_{-0.157}$	8.749 ± 0.006
PTF10qyq	0.160	10592 ± 99	$9.445^{+0.212}_{-0.050}$...
PTF10rab	0.085	11296 ± 70	$7.920^{+1.043}_{-0.114}$	7.811 ± 0.005
PTF10ran	0.160	11127 ± 57	$11.185^{+0.088}_{-0.347}$...
PTF10rhi	0.085	11257 ± 35	$10.014^{+0.077}_{-0.364}$...
PTF10tce	0.041	12362 ± 12	$10.542^{+0.161}_{-0.155}$	8.745 ± 0.053
PTF10tqy	0.045	11568 ± 11	$10.101^{+0.162}_{-0.005}$...
PTF10trs	0.073	11248 ± 2	$10.824^{+0.062}_{-0.070}$...
PTF10trw	0.170	10355 ± 40	$9.387^{+0.259}_{-0.024}$...
PTF10twd	0.073	11646 ± 23	$9.884^{+0.089}_{-0.055}$	8.365 ± 0.006
PTF10ucl	0.080	10541 ± 15	$10.683^{+0.561}_{-0.020}$...
PTF10ufj	0.073	10134 ± 10	$10.789^{+0.428}_{-0.051}$...
PTF10urn	0.110	10972 ± 76	$9.543^{+0.262}_{-0.487}$...
PTF10vfo	0.088	12488 ± 63	$10.751^{+0.011}_{-0.022}$...
PTF10viq	0.034	12480 ± 10	$10.792^{+0.201}_{-0.417}$	8.900 ± 0.013
PTF10wnm	0.066	10910 ± 11	$10.548^{+0.045}_{-0.116}$	8.749 ± 0.044
PTF10wnq	0.069	11681 ± 56	$11.341^{+0.107}_{-0.543}$...
PTF10wov	0.096	10368 ± 27	$10.165^{+0.276}_{-0.076}$...
PTF10wri	0.120	11595 ± 20	$11.777^{+0.101}_{-0.204}$...
PTF10xeb	0.122	9132 ± 62	$7.316^{+0.665}_{-0.091}$...
PTF10xir	0.052	10692 ± 19	$11.025^{+0.428}_{-0.178}$...
PTF10xtp	0.102	10391 ± 103	$10.419^{+0.099}_{-0.133}$...
PTF10ygr	0.115	10177 ± 114	$9.698^{+0.200}_{-0.022}$...
PTF10ygu	0.026	15428 ± 11	$10.911^{+0.491}_{-0.161}$	8.672 ± 0.003
PTF10yux	0.058	11777 ± 19	$10.764^{+0.006}_{-0.066}$...
PTF10zai	0.036	8715 ± 59	$10.822^{+0.563}_{-0.067}$	9.005 ± 0.203
PTF10zak	0.040	11915 ± 10	$10.757^{+0.400}_{-0.157}$	8.997 ± 0.034
PTF10zbn	0.114	9957 ± 249	$11.189^{+0.094}_{-0.160}$...
PTF10zgy	0.044	11056 ± 40	$11.238^{+0.000}_{-0.000}$...
PTF11apk	0.041	10310 ± 10	$10.914^{+0.007}_{-0.164}$...
PTF11bjk	0.140	10613 ± 61	$10.954^{+0.064}_{-0.203}$...
PTF11blu	0.068	10495 ± 35	$9.963^{+0.016}_{-0.081}$	8.605 ± 0.165
PTF11byi	0.039	8625 ± 25	$10.527^{+0.077}_{-0.581}$	8.808 ± 0.094
PTF11ctn	0.079	10156 ± 11	$9.312^{+0.313}_{-0.195}$...
PTF11cyv	0.115	10398 ± 46	$9.851^{+0.100}_{-0.095}$...
PTF11deg	0.063	11724 ± 31	$9.452^{+0.097}_{-0.074}$...
PTF11dws	0.150	12637 ± 45	$11.174^{+0.095}_{-0.308}$...
PTF11dzm	0.041	11232 ± 59	$10.090^{+0.007}_{-0.163}$...
PTF11eot	0.090	11421 ± 50	$8.600^{+0.105}_{-0.135}$...
PTF11fjw	0.193	10684 ± 66	$10.892^{+0.216}_{-0.136}$...
PTF11for	0.128	12106 ± 83	$9.638^{+0.033}_{-0.083}$...
PTF11gdh	0.026	9838 ± 13	$10.390^{+0.190}_{-0.099}$	8.743 ± 0.025
PTF11gin	0.163	11347 ± 42	$9.626^{+0.255}_{-0.546}$...
PTF11gjb	0.125	10601 ± 42	$10.926^{+0.052}_{-0.131}$...
PTF11glq	0.156	9916 ± 166	$11.360^{+0.088}_{-0.019}$...
PTF11gnj	0.131	10341 ± 61	$10.387^{+0.114}_{-0.032}$...
PTF11khk	0.031	9224 ± 11	$10.704^{+0.058}_{-0.120}$	8.926 ± 0.034
PTF11kod	0.188	10519 ± 297	$8.741^{+0.912}_{-0.220}$...
PTF11kpb	0.143	10339 ± 19	$11.675^{+0.091}_{-0.014}$...
PTF11kqm	0.126	10878 ± 21	$10.428^{+0.241}_{-0.030}$...
PTF11kx	0.047	11027 ± 40	$10.315^{+0.169}_{-0.152}$	8.505 ± 0.007
PTF11lbc	0.150	11260 ± 44	$7.967^{+1.320}_{-0.848}$...
PTF11lmz	0.061	13674 ± 21	$11.206^{+0.074}_{-0.203}$...

TABLE 3
SUMMARY OF OUR SAMPLE IN THIS WORK (CONTINUED).

SN Name	Redshift	$v_{\text{Si II}}$ (km s^{-1})	$\log M_{\text{stellar}}$ (M_{\odot})	$12 + \log (\text{O/H})$
PTF11opu	0.065	9791 ± 47	$9.797^{+0.127}_{-0.094}$	8.076 ± 0.050
PTF11qpc	0.089	10632 ± 23	$10.312^{+0.217}_{-0.239}$	8.643 ± 0.123
PTF11qvh	0.133	11042 ± 12	$9.800^{+0.171}_{-0.013}$...
PTF11rke	0.094	12348 ± 35	$9.968^{+0.066}_{-0.136}$...
PTF11rpc	0.143	11907 ± 49	$11.315^{+0.225}_{-0.183}$...
PTF11yp	0.121	8812 ± 41	$11.447^{+0.068}_{-0.313}$...
PTF12awi	0.045	9727 ± 48	$10.503^{+0.133}_{-0.108}$	8.764 ± 0.052
PTF12cdb	0.120	12068 ± 20	$10.877^{+0.212}_{-0.056}$...
PTF12cjd	0.067	11080 ± 17	$9.916^{+0.105}_{-0.131}$	8.615 ± 0.142
PTF12cyd	0.170	11668 ± 12	$9.118^{+0.446}_{-0.073}$...
PTF12czu	0.145	10709 ± 151	$9.005^{+0.021}_{-0.138}$...
PTF12dgy	0.180	9911 ± 23	$10.919^{+0.367}_{-0.175}$...
PTF12dhh	0.057	10701 ± 12	$10.373^{+0.030}_{-0.072}$	8.618 ± 0.032
PTF12dhl	0.057	10441 ± 38	$11.001^{+0.111}_{-0.012}$...
PTF12dhv	0.140	12260 ± 80	$10.442^{+0.144}_{-0.160}$...
PTF12dst	0.192	9385 ± 24	$9.939^{+0.079}_{-0.019}$...
PTF12dwm	0.053	9675 ± 10	$10.538^{+0.159}_{-0.200}$	8.765 ± 0.074
PTF12dxm	0.063	10505 ± 9	$11.033^{+0.005}_{-0.002}$...
PTF12egr	0.132	10490 ± 46	$11.520^{+0.126}_{-0.013}$...
PTF12fhn	0.125	10801 ± 76	$11.281^{+0.142}_{-0.011}$...
PTF12fsd	0.069	10862 ± 25	$10.107^{+0.098}_{-0.117}$	8.398 ± 0.063
PTF12giy	0.029	12093 ± 177	$10.835^{+0.177}_{-0.008}$	8.826 ± 0.096
PTF12gnw	0.100	10077 ± 14	$8.816^{+0.187}_{-0.234}$...
SN 1989M	0.005	12330 ± 50	$10.539^{+0.627}_{-0.144}$...
SN 1994S	0.015	10400 ± 50	$11.113^{+0.036}_{-0.520}$	8.943 ± 0.013
SN 1997Y	0.016	10510 ± 50	$11.018^{+0.067}_{-0.045}$	9.023 ± 0.012
SN 1998dk	0.013	12380 ± 50	$9.982^{+0.033}_{-0.186}$...
SN 1998es	0.011	10240 ± 50	$10.299^{+0.052}_{-0.010}$...
SN 1999aa	0.014	10350 ± 50	$10.533^{+0.132}_{-0.013}$	9.035 ± 0.027
SN 1999ac	0.009	10400 ± 50	$10.254^{+0.504}_{-0.128}$...
SN 1999da	0.013	10660 ± 50	$10.886^{+0.039}_{-0.120}$...
SN 1999dq	0.014	10860 ± 50	$10.941^{+0.422}_{-0.118}$...
SN 1999gd	0.018	10420 ± 50	$10.361^{+0.168}_{-0.044}$...
SN 2000cp	0.034	11000 ± 50	$9.976^{+0.459}_{-0.071}$	8.841 ± 0.026
SN 2000dn	0.032	10190 ± 50	$11.081^{+0.010}_{-0.177}$...
SN 2001bp	0.095	10860 ± 50	$10.602^{+0.065}_{-0.165}$	8.795 ± 0.032
SN 2001da	0.017	11350 ± 50	$10.633^{+0.440}_{-0.185}$...
SN 2001ep	0.013	10160 ± 50	$10.215^{+0.023}_{-0.117}$...
SN 2001fe	0.014	11070 ± 50	$10.341^{+0.109}_{-0.077}$...
SN 2002aw	0.026	10210 ± 50	$10.931^{+0.051}_{-0.076}$	8.976 ± 0.029
SN 2002bf	0.024	13680 ± 50	$10.672^{+0.004}_{-0.004}$...
SN 2002bo	0.004	13070 ± 50	$10.779^{+0.054}_{-0.449}$...
SN 2002cd	0.010	15230 ± 50	$10.971^{+0.124}_{-0.010}$...
SN 2002dk	0.019	10430 ± 50	$11.656^{+0.048}_{-0.151}$...
SN 2002eb	0.028	10230 ± 50	$10.976^{+0.164}_{-0.423}$...
SN 2002eu	0.038	11020 ± 50	$10.648^{+0.493}_{-0.070}$...
SN 2002ha	0.014	10930 ± 50	$11.075^{+0.481}_{-0.198}$...
SN 2003U	0.026	11300 ± 50	$9.670^{+0.614}_{-0.377}$	8.828 ± 0.021
SN 2003Y	0.017	9860 ± 50	$10.728^{+0.153}_{-0.037}$...
SN 2003cq	0.033	12080 ± 50	$11.884^{+0.064}_{-0.111}$...
SN 2003he	0.025	11310 ± 50	$10.335^{+0.545}_{-0.069}$...
SN 2004dt	0.020	13540 ± 50	$10.875^{+0.020}_{-0.144}$...
SN 2004gs	0.027	10430 ± 50	$10.740^{+0.137}_{-0.032}$...
SN 2005M	0.022	10670 ± 60	$9.898^{+0.081}_{-0.030}$	8.504 ± 0.006
SN 2005W	0.009	10600 ± 50	$10.473^{+0.007}_{-0.154}$...
SN 2005ao	0.038	11460 ± 50	$10.915^{+0.161}_{-0.033}$...
SN 2005ag	0.079	11370 ± 50	...	9.250 ± 0.021
SN 2005bc	0.012	10700 ± 50	$10.383^{+0.018}_{-0.120}$	9.054 ± 0.007

TABLE 4
SUMMARY OF OUR SAMPLE IN THIS WORK (CONTINUED).

SN Name	Redshift	$v_{\text{Si II}}$ (km s^{-1})	$\log M_{\text{stellar}}$ (M_{\odot})	$12 + \log (\text{O}/\text{H})$
SN 2005cg	0.032	11560 ± 50	$8.574^{+0.057}_{-0.025}$	7.947 ± 0.039
SN 2005er	0.026	8740 ± 50	$11.478^{+0.492}_{-0.114}$...
SN 2005eq	0.029	10090 ± 50	$11.424^{+0.029}_{-0.452}$...
SN 2005hj	0.058	10550 ± 50	$10.046^{+0.078}_{-0.038}$	8.519 ± 0.038
SN 2005ki	0.020	11030 ± 50	$11.146^{+0.035}_{-0.120}$...
SN 2005ms	0.025	11840 ± 50	$10.684^{+0.210}_{-0.054}$...
SN 2006N	0.014	11300 ± 50	$10.545^{+0.494}_{-0.143}$...
SN 2006S	0.032	10710 ± 50	$10.628^{+0.006}_{-0.184}$...
SN 2006bt	0.032	10510 ± 50	$11.124^{+0.027}_{-0.155}$...
SN 2006bz	0.028	10850 ± 50	$10.471^{+0.006}_{-0.020}$...
SN 2006cm	0.016	11150 ± 50	$10.913^{+0.069}_{-0.047}$...
SN 2006cq	0.048	10160 ± 50	$11.212^{+0.011}_{-0.141}$...
SN 2006cs	0.024	10730 ± 50	$10.913^{+0.490}_{-0.024}$...
SN 2006or	0.021	11340 ± 50	$11.114^{+0.034}_{-0.117}$...
SN 2006sr	0.024	12470 ± 50	$10.778^{+0.325}_{-0.163}$...
SN 2007A	0.018	10600 ± 50	$10.775^{+0.252}_{-0.241}$...
SN 2007N	0.013	10330 ± 50	$10.376^{+0.017}_{-0.141}$...
SN 2007O	0.036	10000 ± 50	$11.033^{+0.007}_{-0.117}$	9.009 ± 0.011
SN 2007af	0.005	10560 ± 50	$9.562^{+0.181}_{-0.096}$...
SN 2007ba	0.038	9630 ± 50	$11.118^{+0.105}_{-0.068}$...
SN 2007bc	0.021	9850 ± 50	$10.922^{+0.020}_{-0.000}$...
SN 2007bz	0.022	11700 ± 50	$9.504^{+0.085}_{-0.100}$	8.329 ± 0.012
SN 2007ci	0.018	11830 ± 50	$10.969^{+0.007}_{-0.150}$...
SN 2007fr	0.051	10740 ± 50	$11.770^{+0.032}_{-0.102}$...
SN 2007gi	0.005	14870 ± 50	$10.643^{+0.479}_{-0.151}$...
SN 2007hj	0.014	11710 ± 50	$10.580^{+0.484}_{-0.143}$...
SN 2007sl	0.027	11370 ± 50	$9.998^{+0.143}_{-0.030}$...
SN 2008Z	0.021	11460 ± 50	$9.488^{+0.203}_{-0.064}$	8.359 ± 0.060
SN 2008ar	0.026	10340 ± 50	$10.880^{+0.071}_{-0.512}$	8.972 ± 0.016
SN 2008sl	0.022	10560 ± 50	$10.559^{+0.129}_{-0.040}$...
SN 2008dx	0.023	8850 ± 50	$10.678^{+0.027}_{-0.136}$...
SN 2008ec	0.016	10750 ± 50	$10.930^{+0.124}_{-0.075}$...
SN 2009an	0.009	12680 ± 50	$10.981^{+0.084}_{-0.000}$	9.086 ± 0.014
SN 2009fx	0.048	10110 ± 50	$10.000^{+0.020}_{-0.170}$...
SN 2009ig	0.009	13660 ± 50	$10.454^{+0.000}_{-0.175}$...
SN 2009no	0.046	10030 ± 50	$10.319^{+0.041}_{-0.187}$	8.776 ± 0.028
SN 2010ex	0.023	10890 ± 50	$10.089^{+0.142}_{-0.030}$...
SN 2010ii	0.027	12240 ± 50	$11.142^{+0.013}_{-0.144}$...
SN 2010iw	0.022	10360 ± 50	$9.731^{+0.066}_{-0.092}$...
SN 2011ao	0.011	10340 ± 50	$9.877^{+0.141}_{-0.032}$	8.481 ± 0.010
SN 2011by	0.003	10270 ± 50	$9.354^{+0.014}_{-0.191}$	8.624 ± 0.022
SN 2011hb	0.029	11800 ± 50	$11.247^{+0.004}_{-0.051}$...
SN 2011ia	0.017	10680 ± 50	...	8.865 ± 0.010
SN 2012bh	0.025	10360 ± 50	$10.538^{+0.406}_{-0.187}$...
SN 2012cg	0.001	10580 ± 50	$8.467^{+0.035}_{-0.160}$	8.729 ± 0.007
SN 2012da	0.018	11110 ± 50	$9.580^{+0.025}_{-0.061}$...
SN 2013di	0.024	11460 ± 50	$11.008^{+0.530}_{-0.060}$...